ADVANCED MATERIALS TECHNOLOGIES
www.advmattechnol.de

Rotary 4D Printing of Programmable Metamaterials on Sustainable 4D Mandrel

*Hesam Soleimanzadeh, Mahdi Bodaghi, Marzieh Jamalabadi, Bernard Rolfe, and Ali Zolfagharian**

This paper presents a novel rotary 4D printing platform capable of producing modular, multi-material, multi-stiffness cylindrical structures directly on a programmable, shape-morphing mandrel. Inspired by bio-inspired re-entrant auxetic geometries, the design incorporates a parametric zigzag pathing strategy to dissipate stress and enhance resilience. The method supports non-planar, continuous-path toolpaths, overcoming the limitations of commercial slicers through a freely available open-source rotary slicing algorithm. Comprehensive numerical and experimental studies to evaluate strain energy distribution, stiffness tunability, and 4D recovery in re-entrant auxetic structures and spiral joints. A data-driven predictive model is introduced to link geometric and material parameters to final shape-morphing behavior, reducing dependence on iterative simulations. The integrated path-planning approach significantly distributes localized Von Mises stress, particularly in hinge regions, while preserving global energy absorption. Using Python scripting within the Grasshopper environment, the complete design-to-G-code algorithm is developed, enabling direct fabrication of non-planar 4D structures, including multi-spiral universal joints with programmable stiffness and multi-degree-of-freedom motion. This work establishes a new paradigm in rotary 4D printing by uniting algorithmic design, stimuli-responsive behavior, and reproducible fabrication within a single open framework. It is concluded by discussing broader implications for sustainable manufacturing, with potential applications in soft robotics, wearable systems, and deployable structures.

1. Introduction

Shape memory polymers (SMPs) combine sustainability with adaptability, enabling the design of engineering structures that mimic nature's flexibility and durability. Over the past two decades, advances in 3D printing have allowed precise layer-by-layer patterning of SMPs, enabling unique biomedical and engineering applications that were previously unattainable.[1] By exploiting the anisotropic properties of SMPs and programming printing parameters, 3D-printed objects can be designed to undergo controlled, stimulus-responsive shape changes.[2] This capability has given rise to 4D printing, where time is integrated as a design factor, allowing structures to either recover their original geometry or transform into programmed shapes. Such developments have opened opportunities in biomedicine, engineering, agriculture, and manufacturing, including multi-stiffness universal mechanical joints produced through non-planar additive manufacturing (AM).[3]

Despite progress in 4D printing, modular and systematic structures for real-world use are still limited. Recent advances in AM have enabled the creation of mechanical metamaterials—a class of architected materials with unique properties rarely found in nature.[4] Through deliberate design, features such as high energy absorption[1] and quasi-zero stiffness[2,5] have been achieved. Growing demands for extreme-environment applications (e.g., aerospace and deep-sea exploration), along with the need for fuel efficiency, cost reduction, and sustainability in aircraft, automotive, and biomedical sectors, have driven interest in multifunctional metamaterials.[6] In particular, metamaterials with tunable elastic properties offer the potential to create smart, sustainable machines that reduce reliance on conventional electronic control systems.[7] Yet, most existing designs remain limited by fixed mechanical properties.[8] A more advanced approach involves reconfigurable metamaterials whose behavior can be altered post-fabrication through external stimuli such as heat or electromagnetic fields, enabling greater adaptability and broader applications.[9]

Correspondingly, several ways for fabricating shape-shifting structures are described throughout the literature.[10] Most rely

H. Soleimanzadeh, B. Rolfe, A. Zolfagharian
School of Engineering
Deakin University
Geelong, VIC 3216, Australia
E-mail: a.zolfagharian@deakin.edu.au
M. Bodaghi
Department of Engineering
School of Science and Technology
Nottingham Trent University
Nottingham NG11 8NS, UK
M. Jamalabadi
Institute for Intelligent Systems Research and Innovation (IISRI)
Deakin University
Geelong, VIC 3216, Australia

The ORCID identification number(s) for the author(s) of this article can be found under https://doi.org/10.1002/admt.202501581

DOI: 10.1002/admt.202501581

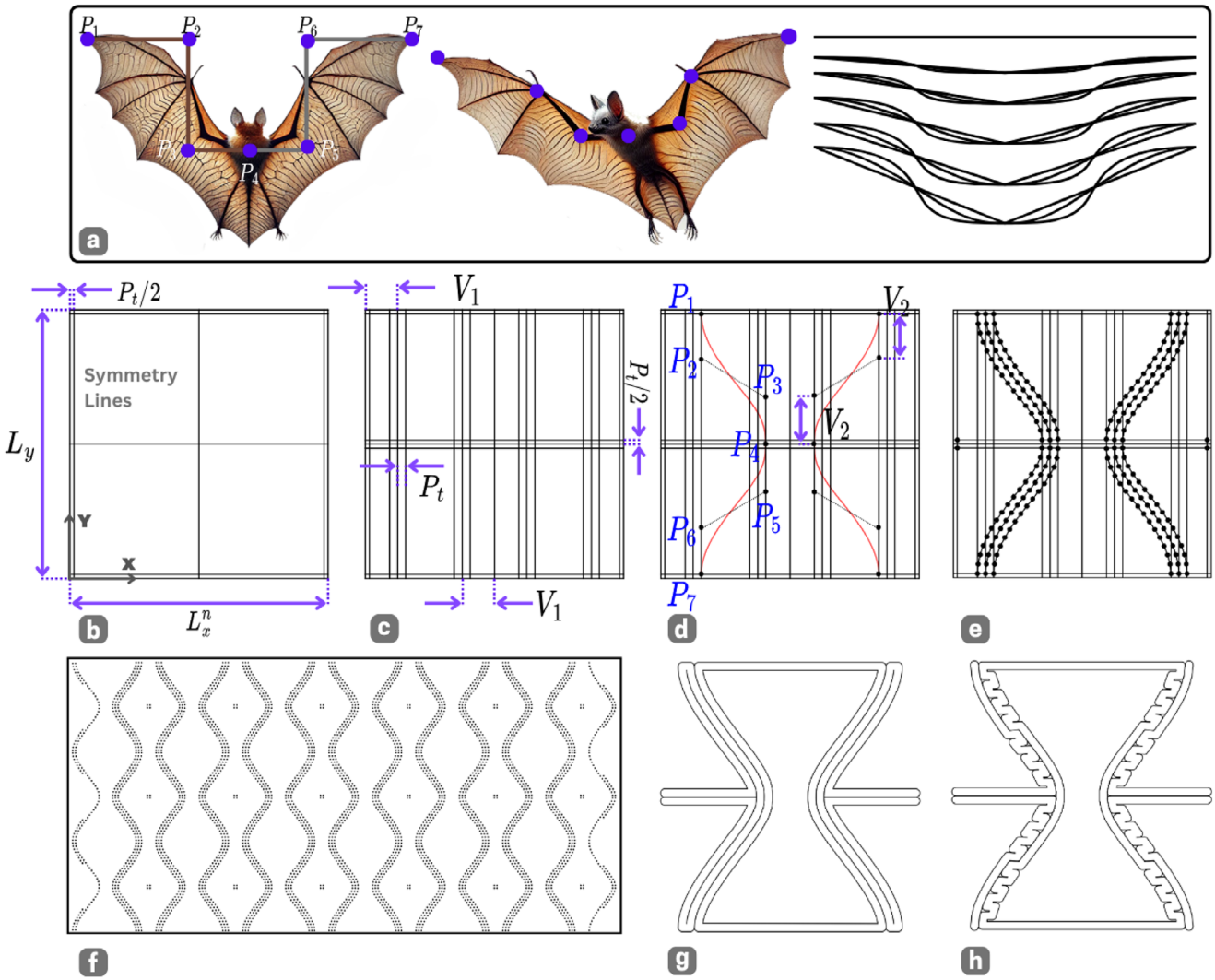

Figure 1. Workflow for parametric design and design-to-G-code generation for a honeycomb re-entrant structure using NURBS control points. a) Seven control points assignments modeled after bio-inspired curves, derived from the structural and aerodynamic properties of a bat wing. b) Specification of individual auxetic unit cell dimensions. c) Establishment of guidelines to facilitate the identification of NURBS control points. d) Construction of the base NURBS curve using seven predefined control points. e) Conversion of printing paths into discrete points, followed by their transformation into polylines. f) Arranging the auxetic pattern along the X and Y directions on the flattened surface of the tubular platform, with N_x and N_y representing the number of patterns in each direction, respectively. g) Representation of the printing path without a specified pattern. h) Representation of the printing path with a zigzag pattern.

on active materials that change dimensions upon stimulation, combined with planar AM methods.[11] In contrast, the potential of fully non-planar 4D printing for shape-shifting metamaterials remains underexplored. To date, research has focused primarily on planar AM of SMPs, overlooking opportunities offered by computational design for complex non-planar geometries. Limited studies on continuous 4D printing show that it can reduce support material waste, yield more homogeneous structures with reliable programming, and enable comprehensive evaluation of adaptivity through numerical methods.

In this regard, Van Manen et al.[12] demonstrated the potential of 4D printing for fabricating reconfigurable metamaterials and devices, with a particular emphasis on tubular 3D printing techniques. Recent work by Le Duigou et al.[13] and Josselin et al.[14] has demonstrated tubular meta-biocomposites fabricated through rotary 3D printing of continuous fiber-reinforced structures, exploiting hydromorphic actuation to achieve controllable rotation, torque, and shape change. While these studies highlight the potential of bioinspired tubular designs, they primarily focus on moisture-responsive actuation of fiber composites, whereas our approach introduces an open-source, path-integrated rotary slicing pipeline for multi-material auxetic metamaterials with programmable, support-free toolpaths.

Byrne et al.[15] examined the use of 3D printing for tubular soft robots, highlighting the potential for enhanced flexibility and adaptability in robotic applications. Several studies have also investigated rotary mandrel 3D printing and the influence of process parameters. Guerra and Ciurana[16] fabricated

polycaprolactone stents with a closed-diamond pattern using a rotating mandrel, analyzing how printing settings affected dimensional accuracy and material distribution. Similarly, Zhao et al.[17] produced PLA-based stents via FDM on a rotary mandrel, optimizing rotation speed, temperature, printing speed, and nozzle-to-mandrel distance. Singh et al.[18] further demonstrated the potential of FDM with a rotating mandrel for manufacturing bioresorbable stents, improving precision and overcoming the limitations of traditional planar 3D printing.

Researchers have optimized auxetic cells using FEM methods,[19] isogeometric design,[20] and deep learning-enhanced algorithms[21] to fully characterize 4D-printed re-entrant unit cells. Both direct[22] and passive[23] 4D programming of cylindrical auxetic re-entrant patterns have been explored to enhance adaptability, while[24] investigated the shape-shifting dynamics of tubular re-entrant structures, focusing on recovery time under varying parameters. These studies highlight the tunable properties of auxetic metamaterials and their adaptability across applications. Numerous works,[25–30] further demonstrate their versatility in biomedical devices, soft robotics, and aerospace engineering.

It is worth mentioning that compared with photopolymerization-based methods such as DLP, the proposed rotary 4D printing pipeline offers several practical advantages. First, it eliminates the need for support structures during tubular fabrication, thereby reducing both material waste and printing time. Second, the approach is more cost-effective, as it relies on widely available FDM facilities and a broader range of sustainable, bridgeable filaments such as PLA. Third, the continuous, fiber-like toolpaths generated by our algorithm provide mechanically stronger interfaces than voxel-based DLP fabrication, where inter-layer bonding can be weaker. Taken together, these features make the method more accessible, economical, and mechanically robust for fabricating programmable tubular metamaterials.

However, no prior studies have demonstrated a fully sustainable, parametrically designed non-planar 4D printing approach using ready-to-use 3D printers that also incorporate path strategies to minimize failure during shape-shifting. To address this gap, we introduce a rotary 4D re-entrant mandrel capable of adapting its dimensions, serving as a versatile platform for tubular 4D printing. This adaptive mandrel eliminates the need for additional supports, enabling efficient and customizable fabrication on diverse geometries. By integrating the auxetic mandrel directly into the 4D printing process, our method provides a self-contained, sustainable, and practical solution for tubular 4D applications.

In this study, we present a parametric non-planar path-to-G-code design algorithm that enables flexible and adaptive fabrication of diverse tubular structures. Implemented in Python within the Grasshopper environment, the workflow ensures full customizability and extensibility, allowing users to generate tubular G-code for auxetic patterns and varied printing parameters without relying on commercial slicers, which are not available for rotary 3D printing. By facilitating seamless customization of design parameters, the algorithm offers a versatile and precise tool for tubular 4D printing, representing a significant step toward advanced non-planar fabrication.

We further integrate a mounted zigzag design path into the auxetic rotary 4D mandrel, as path-level control in 4D printing enables effective stress redistribution within tubular metamaterials. Unlike conventional slicers, this functionality has not been available in any open-source or commercial software for non-planar structures. The path-controlled design allows the mandrel to accommodate a wide range of shapes and diameters without compromising integrity or risking failure, while dynamically adapting to external stimuli. In addition, we introduce an adaptive rotary 4D printing platform that supports multi-material integration and multi-stimuli responsiveness within a single fabrication process. By combining thermally and magnetically responsive materials with continuous non-planar path planning, the platform enables programmable cylindrical structures with complex motion and tunable properties. The integration of bioinspired auxetic geometries and embedded zigzag paths ensures real-time adaptability, while the open-source slicer provides extensibility and reproducibility across applications.

The structure was analyzed using FEM, accounting for both instantaneous hyperelastic behavior and time-dependent viscoelastic deformation of PLA. Strain energy evaluation at both nodal and global levels showed that the zigzag-integrated design reduced localized stress accumulation by ≈36% while maintaining comparable total energy absorption. Compared with a re-entrant design without path control, the zigzag path effectively redistributed stress away from hinge regions, preventing failure during activation. These results demonstrate how optimized path design enhances the integrity and durability of shape-shifting materials under load. In addition, a data-driven predictive model was introduced to correlate geometric and material parameters with 4D deformation outcomes, reducing reliance on repeated FEM simulations. Overall, the PLA re-entrant metamaterial cylinder provides a sustainable tubular printing platform with the ability to dynamically change diameter and achieve rapid shape recovery.

The 4D-printed tubular re-entrant auxetic platform was further used to fabricate a PLA spiral universal joint with tunable stiffness, demonstrating the versatility of the developed approach. Unlike recent studies on tubular 4D printing, our method introduces an open-source, path-integrated rotary slicing framework that enables support-free fabrication, dual-material integration, and programmable toolpaths. Leveraging parametric design and shape-shifting properties, the spiral joint adapts its mechanical response to external conditions. FEM and experimental studies confirmed the tunability and stability of the structure under magnetic and thermal stimuli. These results highlight how the proposed platform advances beyond prior rotary approaches by enabling multifunctional, adaptable 4D-printed joints with direct applications in engineering and biomedicine.

2. Tunable Re-Entrant Rotary 4D Mandrel

Materials and structures exhibiting a negative Poisson's ratio, known as auxetic materials, display exceptional mechanical properties. Under uniaxial compression, these structures experience lateral contraction, a behavior opposite to most conventional materials. In this context, a re-entrant auxetic shape is chosen to

achieve a negative Poisson's ratio, ensuring that the volume increases when the metamaterial undergoes expansion.[31] This design allows for the adjustment of the tubular auxetic metamaterial's diameter, enabling it to function as a fully adjustable and sustainable rotary mandrel.

2.1. Design

To enhance control over the diameter range of the proposed auxetic mandrel, one of our objectives is to increase the adaptability of auxetic structures. This is achieved by minimizing the number of input variables while optimizing geometric design parameters that dictate the cylindrical shape properties. To achieve this, a re-entrant honeycomb auxetic cell is initially designed, inspired by biological principles. Specifically, bioinspired cubic NURBS (Non-Uniform Rational B-Splines) curves[32] derived from the wing structures of bats, as shown in **Figure 1a**, are employed due to their ability to provide C^2 continuity, ensuring smooth deformation even under large strains. This is particularly crucial when the structure experiences significant changes in diameter.

The selection of bat wings was made anecdotally, inspired by their ability to undergo significant joint and skeletal deformations while preserving the arc length of the structure. This analogy helped us conceptualize the use of control points to mimic joint flexibility and guided the implementation of a NURBS-based framework capable of generating diverse auxetic geometries with smooth, length-preserving transitions. While not a direct mechanical model, the bat-wing observation served as a useful conceptual analogy to motivate our parametric approach.

To achieve this, we first flattened the tubular printing platform to facilitate the calculation of the dimensions for each unit cell. The width of each unit cell can then be computed using the following relation

$$L_x^n = \frac{\pi(D_p + 2P_h n)}{N_x} = \frac{\pi D_L}{N_x} \tag{1}$$

where L_x^n, P_h denote the length of each cell in n^{th}layer, and layer height, respectively. D_p represents the diameter of the initial cylindrical printing platform, D_L the diameter of the current layer, and N_x denotes the number of unit cells in the honeycomb re-entrant auxetic structure along the x-direction. Next, as illustrated in Figure 1b, the unit cell is constructed using the input variables N_x, L_y, and P_t, where P_t represents the printing thickness of each layer. To fully define the 4D printing behavior during the 3D printing process, three layers of printing will be included in each re-entrant curve. As shown in Figure 1c, the guidelines for drawing the honeycomb re-entrant NURBS are determined using an offset variable V_1, which can be calculated as follows,

$$V_1 = \overline{V_1} \cdot \frac{L_x^n}{2} \tag{2}$$

where $0 \leq \overline{V_1} \leq 1$ is an input design variable named as the normalized offset value.

To complete the parametric design of the honeycomb re-entrant structure, seven control points are defined based on the guidelines, introducing a new variable V_2, as shown in Figure 1d,

$$V_2 = \overline{V_2} \cdot \frac{L_y}{4} \tag{3}$$

where $0 \leq \overline{V_2} \leq 1$ is an input design variable named as normalized curvature value. The proposed NURBS equations, derivation methods, and detailed specifications of the control points are provided in Note S1 (Supporting Information).

Next, for the purpose of generating points to construct the G-code, the NURBS curve will be offset and mirrored along the symmetry lines shown in Figure 1b. These curves will then be segmented into 3D printing path points by defining an arbitrary division value N_p, producing a finite number of polylines, as illustrated in Figure 1e. In the following step, the generated points are arranged along the X and Y directions on the flattened tubular platform, with N_x and N_y indicating the number of patterns in each respective direction, as illustrated in Figure 1f.

Here, we propose a novel approach to enhance the deformability of 4D-printed tubular structures by optimizing stress distribution away from hinged regions and toward other areas. To achieve this, we explore various point placements and clustering during the printing process to generate alternative printing paths. In this paper, we introduce an algorithm to create diverse path patterns, with a focus on a zigzag pattern generated by strategically dividing NURBS curves into appropriate segments, as shown in Figure 1h.

The zigzag pattern is optimized to distribute bending, compression, and tensile stresses across multiple focal points, minimizing stress concentrations and reducing the likelihood of fractures and structural failure. This design enhances the overall durability and mechanical integrity of the structure. This method aims to improve the structural flexibility and performance of the tubular design. For different path patterns, the number of divisions, N_p, should be calculated to ensure the optimal shape is achieved without leaving any void or overlap spaces. For the zigzag pattern, N_p is calculated by dividing the printing thickness by the length of the curve, as shown below:

$$N_p = \left[\frac{\int_{u_0}^{u_n} \frac{\partial C(u)}{\partial u} du}{P_t} \right] \tag{4}$$

where u_0 and u_n are the bounds of the parameter u, typically defined by the start and end knots, and $C(u)$ denotes NURBS equation described in Note S1 (Supporting Information).

2.2. NURBS Symbolic Regression

The theoretical and numerical computation of Equation (4) is computationally intensive and time-consuming, making this class of well-optimized curves less attractive for many researchers. In our NURBS curve formulation, six dependent variables influence the final shape: D_L, N_x, P_t, L_y, $\overline{V_1}$, and $\overline{V_2}$. The first five variables control the size of the curve within a unit cell, as well as its stretching and compression characteristics. In contrast, $\overline{V_2}$ governs the smoothness and curvature of the NURBS.

It is important to note that alternative classes of curves may yield different shapes, typically involving only the first five variables. One of our primary objectives is to estimate the governing equations of the NURBS curve to enable more efficient computations. To achieve this, we employed Symbolic Regression (PySR), which, unlike traditional regression methods that fit data to a predefined model, explores the space of mathematical expressions to identify the model that best describes our data without requiring the complexity of a full neural network. We provided the model with 300 data points sampled from the NURBS, determined by all variables except $\overline{V_2}$. Given our hypothesis that the equation may involve trigonometric functions, we included a range of functional forms—polynomial, Gaussian, sigmoid, exponential, and sinusoidal—in the algorithm. The algorithm then minimizes the mean squared error (MSE) to identify the optimal model. Ultimately, the resulting equation was found to be sinusoidal, as follows:

$$C(u) \approx \frac{\pi D_L}{2N_x}\left[1 - 2\overline{V_1}\right] sin\left(\frac{\pi}{L_y - P_t}u\right) \tag{5}$$

where $0 \le u \le L_y - P_t$.

Subsequently, to calculate the arc length of $C(u)$ for use in Equation (4) and to further determine the Poisson's ratio and relative density of the auxetic structure, we applied Simpson's rule to the Equation (5). We then calculated the curve lengths by integrating the derived equation and compared the results with the true lengths obtained from numerical simulations in Grasshopper. This comparison revealed a discrepancy, leading us to conclude that the influence of $\overline{V_2}$ cannot be neglected. In response, we updated the PySR model by incorporating polynomial terms and using both the curve lengths calculated from the Equation (5) and $\overline{V_2}$ values, along with other relevant features, as inputs. The true arc length of the NURBS, calculated from 32,400 data points, was provided as the output. Given the true values, PySR generated the following equation for calculating the curve length, achieving an R-squared error of 0.9995:

$$C_L = \left(1 - \frac{\overline{V_2}}{4}\right)\left(\left(L_y - P_t\right)^2 + \left(\frac{\left(1 - 2\overline{V_1}\right)\pi D_L}{N_x}\right)^2\right)^{\frac{1}{2}} + \left(\frac{\overline{V_2}}{4}\right)\left(L_y - P_t + \left(1 - 2\overline{V_1}\right)\frac{\pi D_L}{N_x}\right) \tag{6}$$

and consequently, the Equation (4) can be rewritten as:

$$N_p = \frac{C_L}{P_t} \tag{7}$$

Since the mechanical properties of a structure are inherently linked to its relative density, **Figure 2** presents a comparison of the influence of key variables on the relative density of auxetic metamaterial structures. This comparison highlights how changes in structural parameters affect the overall mechanical behavior. The detailed formulation and derivation of the auxetic metamaterials are provided in Note S2 (Supporting Information), offering insights into the relationship between design variables and their impact on the mechanical performance of the metamaterials.

2.3. Tubular G-code Algorithm

Currently, there is no commercially available software designed to generate non-planar G-code for hobbyist FDM 3D printers. In response to this gap, we propose a direct design-to-G-code algorithm using Grasshopper. The algorithm first generates auxetic patterns based on user-defined printing parameters, and then automatically generates the corresponding G-code tailored to specific user inputs. This streamlined approach simplifies the process of creating non-planar prints, making it more accessible for a wider range of users. To achieve this objective, the algorithm depicted in **Figure 3** is designed as a recursive process for each layer, enabling users to specify distinct printing parameters and paths for each layer, thus facilitating the programming of 4D behavior in 3D-printed polymers. As illustrated, the algorithm begins by accepting user inputs, including parameters such as printing head travel speed, feed rate for active and passive layers, printing temperature for active and passive layers, filament diameter, and additional aforementioned variables D_p, P_h, P_t, n, L_y, N_x, N_y, $\overline{V_1}$, $\overline{V_2}$, and O. These inputs guide the layer-by-layer modification of the G-code, enabling precise control over the 4D properties of the printed structure. The algorithm, provided in Algorithm S1 (Supporting Information), generates various honeycomb auxetic shape patterns within the Rhino environment while simultaneously producing tunable G-code within the Grasshopper environment. This integrated approach allows for seamless pattern generation and G-code customization, facilitating the precise programming of desired 4D behaviors in the final printed structure.

Furthermore, the algorithm is capable of generating tunable shape-morphing patterns through a 2D gradient of $\overline{V_1}$ and $\overline{V_2}$ variables, as illustrated in **Figure 4**. The auxetic flattened pattern can be adjusted to exhibit various shape-morphing phases. In this paper, we focus on the cylindrical auxetic shape with constant variables, serving as a foundational study for further advancements in non-planar 4D printing of tunable shape-morphing patterns. This approach lays the groundwork for future exploration of dynamic, programmable morphing structures in complex geometries. More details about the proposed algorithm and its workflow can be found in Note S3 (Supporting Information).

To generate the 2D gradient of the auxetic cell map, we employed a customized function defined by the two input variables, $\overline{V_1}$ and $\overline{V_2}$. Each panel in the array ($N_x \times N_y$) was assigned a value determined by its local $\overline{V_1}$ and $\overline{V_2}$ coordinates, while all other design coefficients were kept constant. The parameters used in Figure 4 are the same as those listed in **Table 1**, except for $N_x = 8$. Both $\overline{V_1}$ and $\overline{V_2}$ were varied linearly across their domains, normalized between 0 and 1, to span the minimum and maximum gradient values. Finally, for each panel, the extracted values were applied to the governing equations, directly influencing the curvature of the auxetic re-entrant NURBS design.

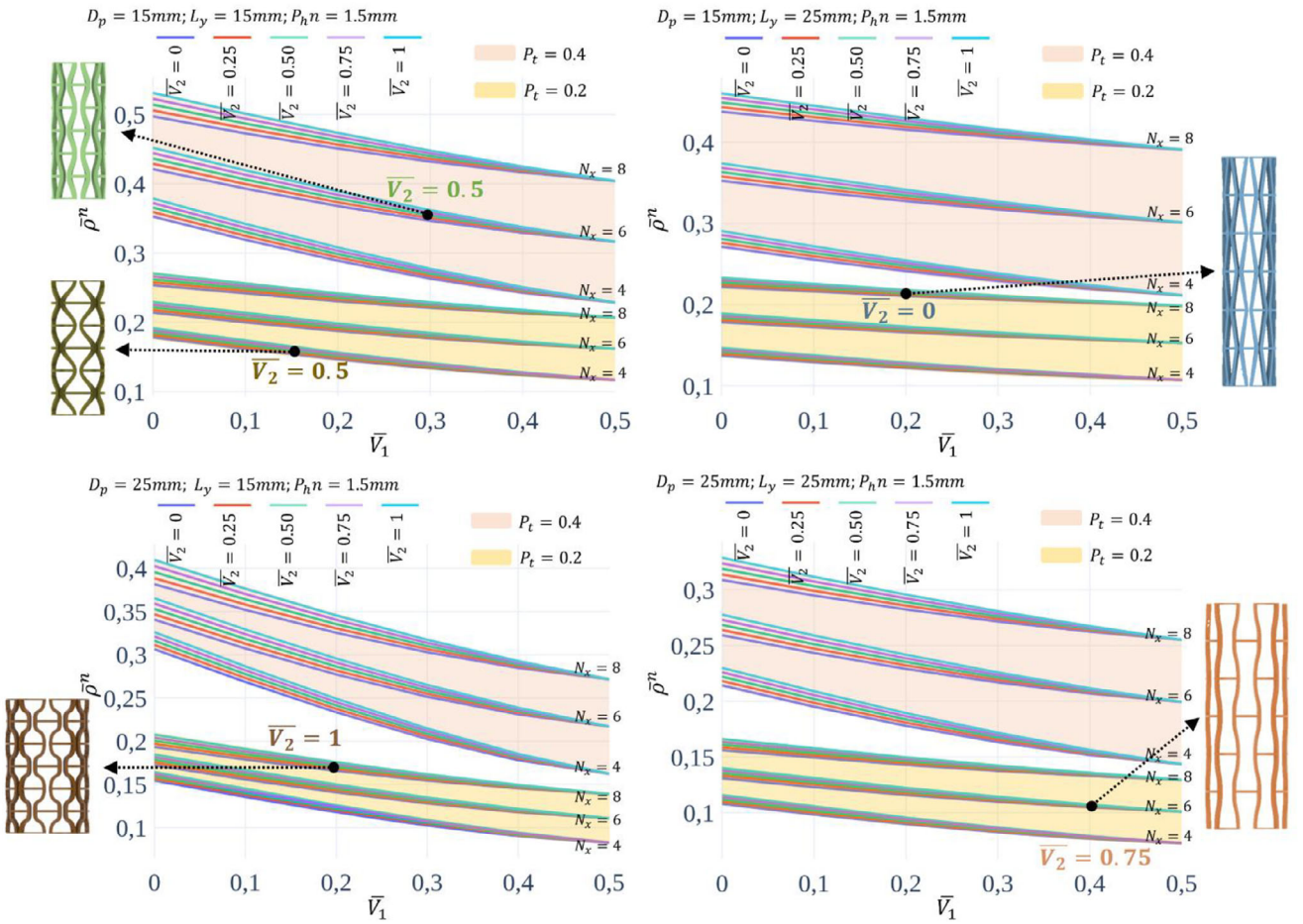

Figure 2. A comparative analysis of the Influence of key variables on the relative density of auxetic metamaterial structures with constant thickness ($P_h n$) of 1.5 mm.

2.4. Fabrication

Since there is no commercially available software or 3D printer specifically designed for tubular 3D printing, we utilized the Snapmaker 2.0 A350 3-in-1, a widely accessible commercial printer, making our proposed algorithm usable for both researchers and hobbyist 3D printers without any hardware modifications. **Figure 5** shows a schematic of the printer and process. The non-planar fabrication of the auxetic honeycomb re-entrant structure is demonstrated in Supplementary Videos S1 and S2 (Supporting Information), while a small-scale auxetic metamaterial, 3D-printed using this algorithm, is shown in Supplementary Video S3 (Supporting Information). Further details on the hardware and fabrication process are provided in Note S4 (Supporting Information).

2.5. Numerical and Experimental Characterization

2.5.1. FEA

To perform FEA for characterizing the behavior of tunable re-entrant auxetic metamaterials, it is essential to first accurately characterize the mechanical properties of the PLA material. Materials typically exhibit both instantaneous and time-dependent responses, necessitating a combination of elastic and viscoelastic models to capture their behavior. Classical viscoelasticity models, such as the Kelvin-Voigt and Maxwell models, represent material responses using springs (for elastic behavior) and dashpots (for viscous behavior). In its glassy phase, while undergoes large strains, PLA initially responds in a manner that can be modeled as hyperelastic,[38] capturing its immediate deformation behavior through an instantaneous modulus. As the material undergoes relaxation over time, its response becomes viscoelastic,[39] which governs its long-term deformation characteristics and time-dependent modulus. Therefore, a combination of hyperelastic and viscoelastic models is required to accurately describe the full mechanical behavior of PLA under different loading conditions.

To consider instantaneous behavior of PLA, the hyperelastic models' full incompressibility is assumed in fitting the hyperelastic constants to the test data. As discussed in.[38] the Yeoh model,[40] which represents the hyperelastic reduced polynomial form for N = 3, provides the best fit for the mechanical behavior of PLA with 100% infill[41]. To account for the viscoelastic behavior of PLA, a suitable mathematical model must be

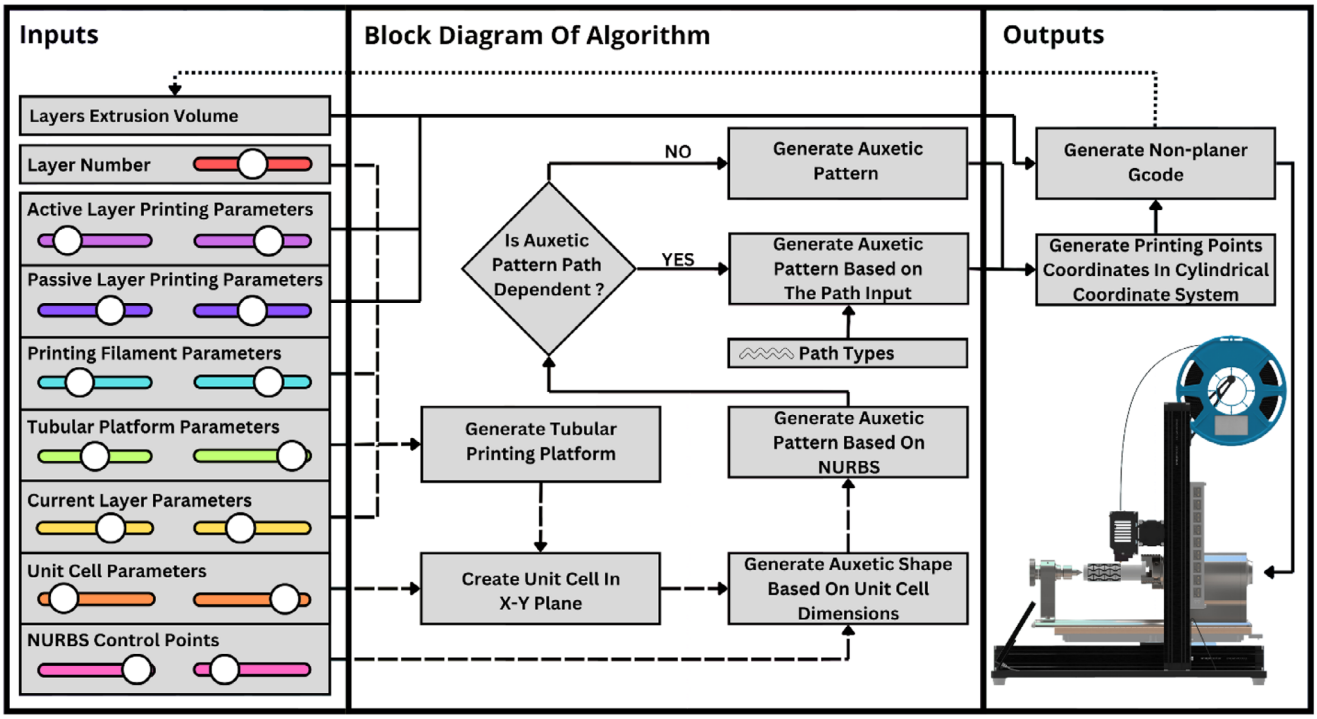

Figure 3. Flowchart of grasshopper design-to-G-code algorithm to generate tubular G-code for parametric cylindrical honeycomb re-entrant auxetic patterns.

integrated with the Yeoh model to incorporate the material's time-dependent response[42]. A key phenomenon observed during long-term loading is stress relaxation, where the material's stiffness, both deviatoric and volumetric, decreases while the strain remains constant. The Prony series is widely recognized as an effective mathematical formulation to describe this behavior, allowing for accurate modeling of the time-dependent reduction in stiffness during sustained deformation.[36] The characterization of the material, encompassing both instantaneous hyperelasticity and time-dependent viscoelasticity, along with FEA details are detailed in Note S5 (Supporting Information).

2.5.2. Poisson's Ratio

To thoroughly characterize the behavior of a re-entrant auxetic metamaterial during diameter changes caused by the reorientation of polymer chains as the material transitions to the glassy phase of PLA, we first theoretically calculate the structure's Poisson's ratio. To address the limitations of existing research on re-entrant auxetic metamaterials,[33–37] which typically derive Poisson's ratio formulations for specific geometric configurations independently, we propose a unified approach. Moreover, limited research has explored the impact of parametric design, such as the application of sigmoid functions,[31] on the geometric characterization of re-entrant auxetic metamaterials. A comprehensive formulation that correlates all design variables to the final geometric configuration has yet to be established. In this context, it becomes feasible to investigate the influence of individual design parameters by analyzing their respective contributions to the arc length of curves, as outlined in Equation (6). This approach enables a deeper understanding of the role each parameter plays in shaping the final structure.

In this study, we introduce a single parametric relation that can predict the Poisson's ratio across varying geometrical inputs without the need to monitor ligaments angular changes during deformation. This generalized formulation streamlines the analysis by classifying the relevant parameters into three categories: constants, independent variables, and dependent variables. This systematic grouping allows for a more efficient and comprehensive prediction of the auxetic behavior under diverse geometric conditions.

As previously discussed, we have identified six independent variables: D_L, P_t, L_y, N_x, N_y, $\overline{V_1}$, and $\overline{V_2}$. During deformation, it is evident that P_t, N_x, and N_y remain constant. Through a detailed observation of the system's behavior, we also conclude that $\overline{V_2}$, which is associated with the curvature of the curves, remains unchanged. However, as the input variable D_L(diameter) changes, both L_y and $\overline{V_1}$ are affected, indicating their dependence on the variation of D_L. This relationship is crucial for understanding the dynamic behavior of the system under deformation. Details on the formulation of Poisson's ratio are provided in Note S6 (Supporting Information).

To validate the proposed formulation, a combination of experimental testing and FEA was performed. As illustrated in **Figure 6a**, a specimen with a thickness of 1.5mm and an initial diameter of 30mm, along with other geometrical dimensions detailed in the Figure 6a, was subjected to deformation. The printing parameters, as listed in Table S1 (Supporting Information),

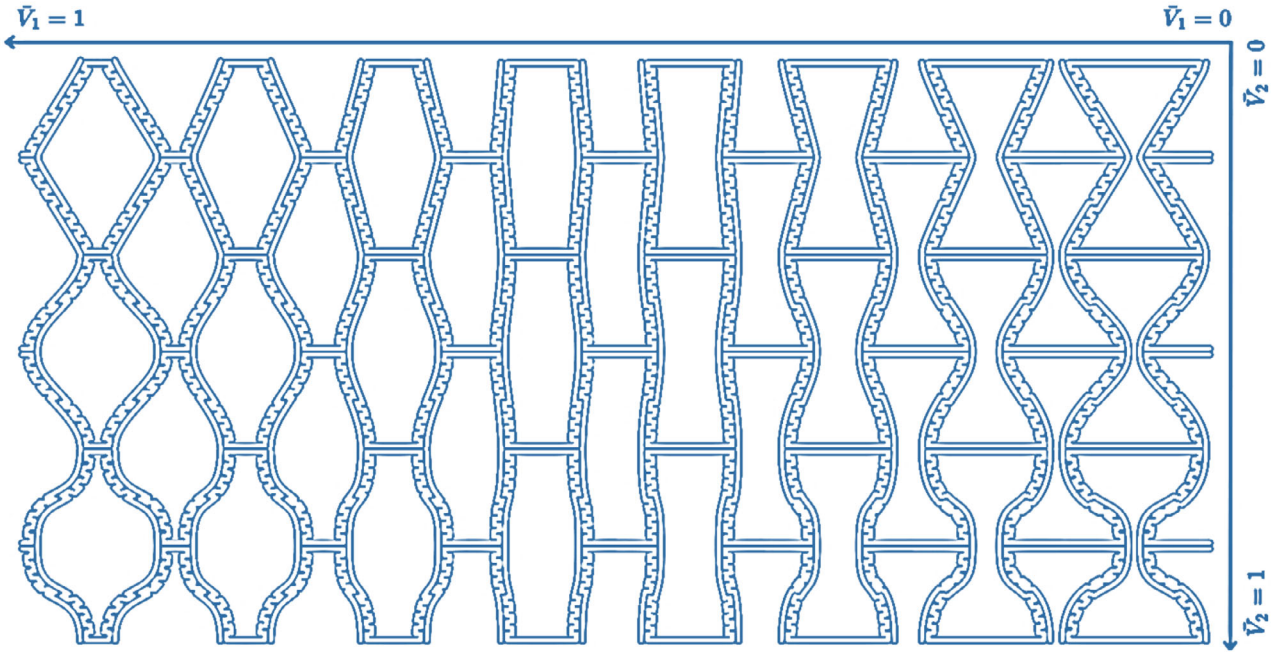

Figure 4. 2D gradient of auxetic cell mapping using independent variables of $\overline{V_1}$ and $\overline{V_2}$.

Table 1. Specimens' 3D printing dimensions utilized in shape recovery experiments.

Parameters	Name	Value
D_p	Platform Diameter	30 mm
P_h	Printing Layer Height	0.1 mm
P_t	Printing Layer Thickness	0.6 mm
n	Number of Layers	15
N_x	Pattern Repetition Toward X direction	5
N_y	Pattern Repetition Toward Y direction	3
L_y	Height of Auxetic cell	20 mm
$\overline{V_1}$	Normalized Offset Value	0.15
$\overline{V_2}$	Normalized Curvature Value	0.5

were used to manufacture the specimen. During testing, the specimen exhibited a diameter change from 30mm to 48mm, where it approximately achieved its maximum Poisson's ratio. Notably, this occurred when the metamaterial reached $\overline{V_1'} = 0.5$.

The theoretical simulation is provided in Algorithm S1 (Supporting Information) through numerical simulation cluster, where the aforementioned formulations are applied to model the deformation of the cylindrical auxetic structure as it approaches its glassy phase. Both FEA and experimental testing were performed across different values of normalized curvature $\overline{V_2}$ and N_x, as depicted in Figure 6b. In the FEA simulations, buckling was observed in the ligaments at the top and bottom regions of the structure (Figure 6c), resulting in a slight deviation from the theoretical predictions. This buckling effect, however, does not

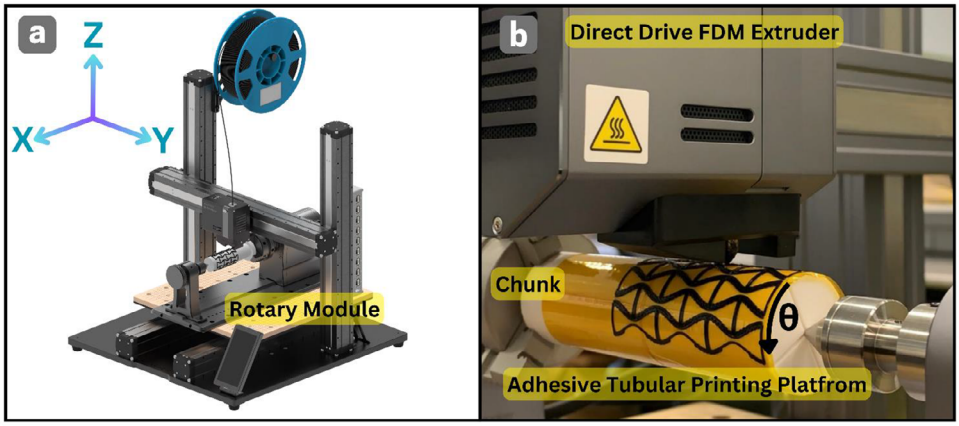

Figure 5. Configuration and integration of a commercial FDM 3D printer with a rotary module for enhanced fabrication flexibility. a) The 3-in-1 Snapmaker 3D printer. b) The rotary module and setup utilized to perform non-planer 3D printing.

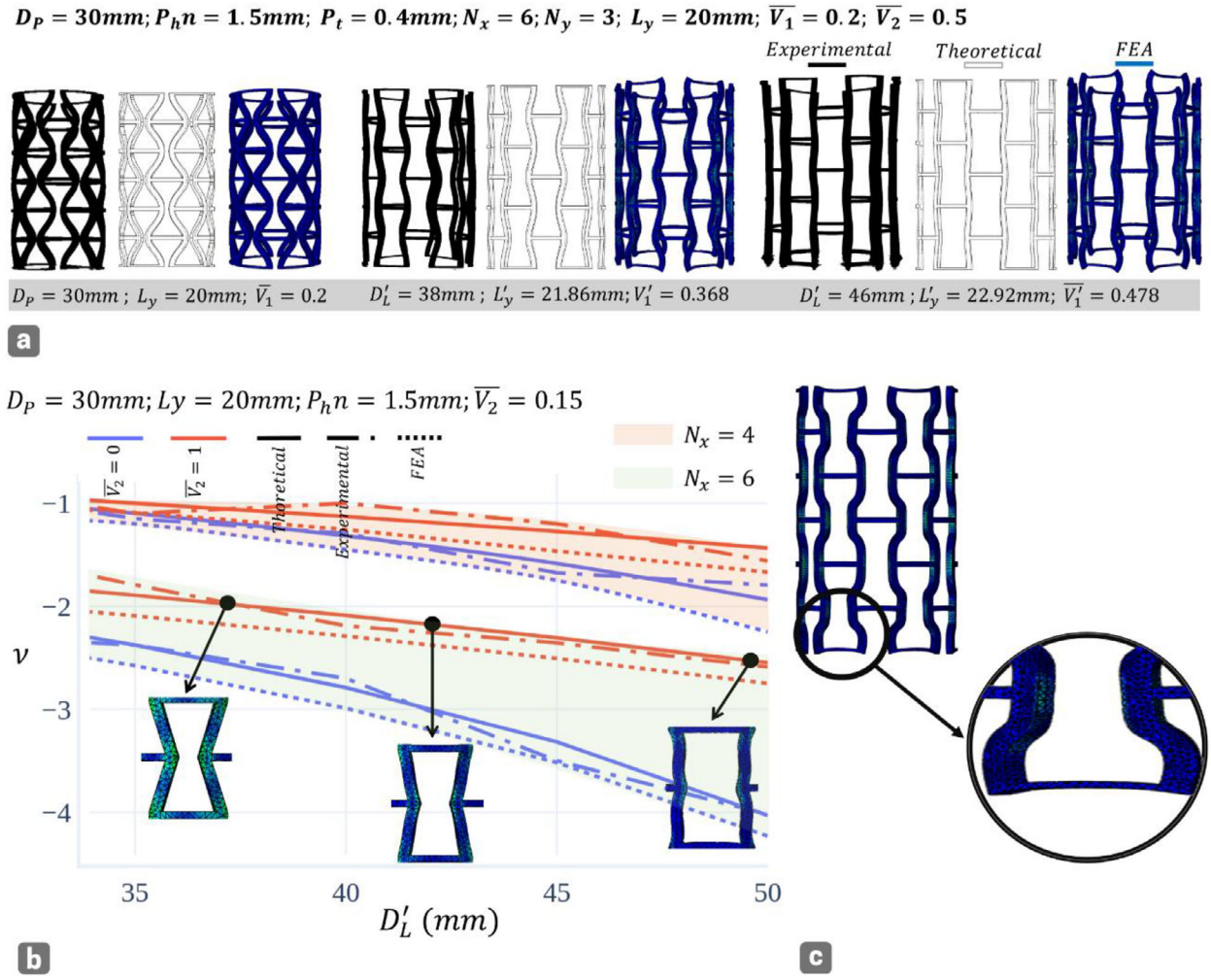

Figure 6. Characterization of Poisson's Ratio for parametric NURBS re-entrant auxetic metamaterials. a) Theoretical, FEA, and experimental schematics illustrating the deformation of the auxetic structure during 4D deformation. b) Comparative analysis highlighting the influence of key parameters on the Poisson's ratio of the auxetic metamaterial structure, with a constant thickness (P_hn) of 1.5 mm. Data shown as mean ± SD (n = 3 specimens). No formal hypothesis testing was performed. c) Observation of pure buckling in the connecting ligaments during deformation.

occur as prominently in physical experiments in all ligaments. Consequently, the experimental results typically fall between the theoretical predictions and FEA simulations, highlighting the complex interaction between material behavior and structural constraints.

Experimental tests and FEM simulations in Abaqus showed good agreement, confirming that deformation occurred without significant buckling artifacts. Minor local effects at the upper and lower ligaments were observed but were negligible. The theoretical formulation based on pure geometric deformation also accurately predicted both the deformation and Poisson's ratio, further validating that the negative Poisson's ratio is a structural effect rather than a result of instability.

2.5.3. Path-Dependent Stress Distribution

As discussed in previous sections, the proposed algorithm facilitates the integration of path planning into parametric re-entrant NURBS auxetic cell designs. In this paper, we have introduced a zigzag algorithm for 4D printing, capable of adapting structural configurations under varying external stimuli, such as thermal effects.

Figure 7a illustrates the Von Mises stress distribution in a conventional cylindrical auxetic structure without the inclusion of a path, by imposing maximum Von Mises stress bounds during induced deformation through radial displacement from an initial diameter of 30 to 48 mm in T_g = 61.5 °C. In contrast, Figure 7b demonstrates how incorporating a zigzag path into the re-entrant auxetic structure redistributes the stress concentration from the hinge regions to the broader structure. This effect is further corroborated in Figure 7c, which shows the results of FEA simulations on 50 specimens with and without the path. The analysis indicates a significant reduction in the maximum Von Mises stress when the path is included in the printed structures. Figure 7d presents a printed specimen with the zigzag path, showcasing the algorithm's precision and the successful implementation of Equation (7) in 3D printing this class of

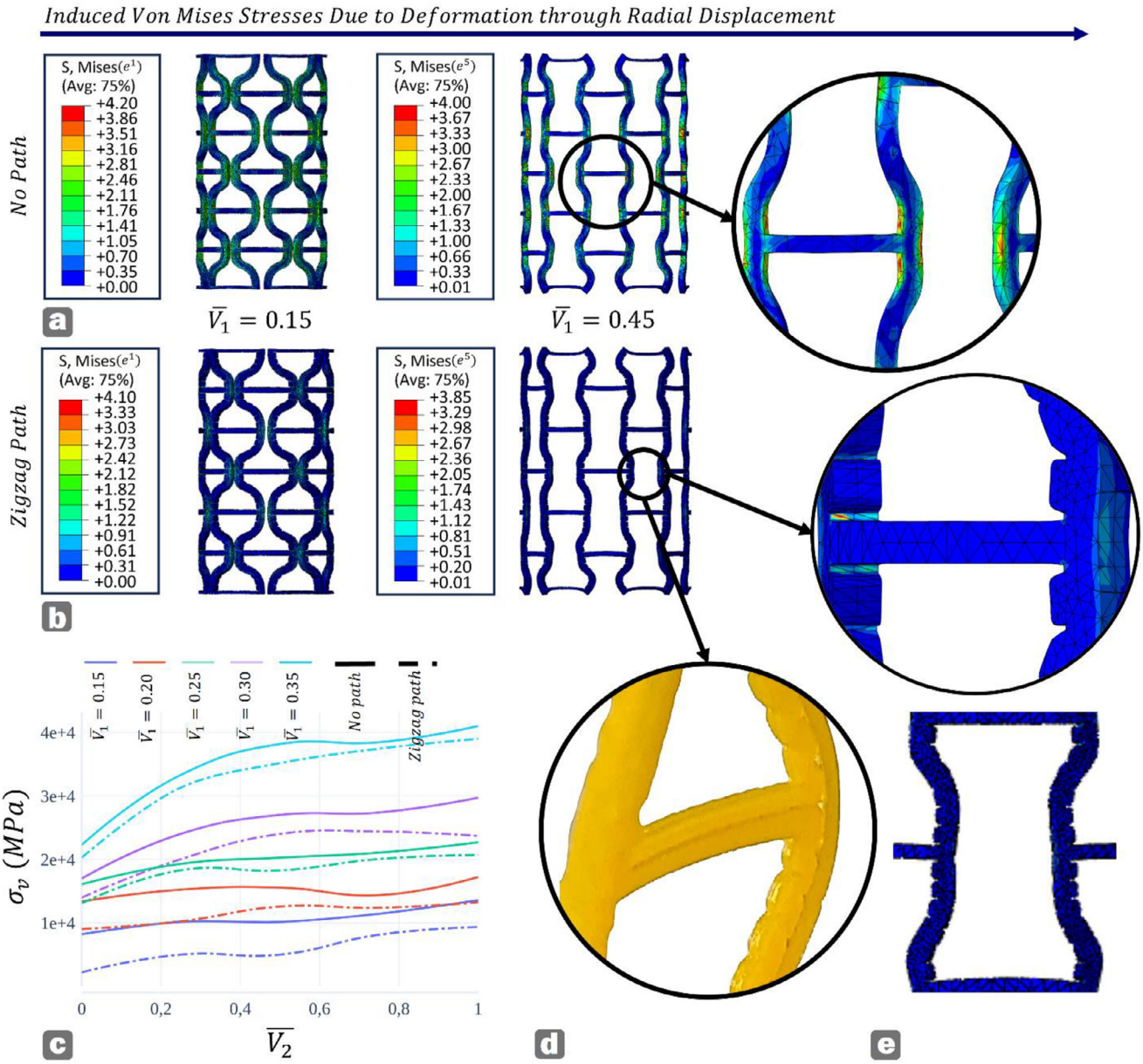

Figure 7. Impact of zigzag path inclusion on stress distribution throughout a cylindrical structure, particularly in the hinge region. a) Von Mises stress distribution in a conventional cylindrical auxetic structure without path inclusion. b) Von Mises stress distribution in a cylindrical auxetic structure with path inclusion, demonstrating the redistribution of stress. c) FEA simulations performed on specimens to evaluate the effects of path inclusion under varying parameters. d) A 3D printed specimen incorporating the zigzag path, highlighting the precision of the algorithm and the successful application of the path. e) The auxetic cell used in FEM simulations post-deformation.

structures. Finally, Figure 7e highlights the inclusion of the path in FEA simulations in an auxetic cell, accurately capturing the behavior of re-entrant auxetic metamaterials under deformation.

2.5.4. Shape Morphing Behavior

In this study, we investigated the shape memory behavior of 4D-printed PLA parametric re-entrant auxetic metamaterials by heating the metamaterial shell, with dimensions specified in Table 1, in hot water until it reached its T_g = 61.5 °C. Subsequently, the structure's diameter was altered to 35 mm, as demonstrated in Video S4 (Supporting Information). The shape recovery rate and shape fixing rate of stents were recorded and analyzed, as shown in Supplementary Videos S5 and S6 (Supporting Information). The shape memory performance of the 4D-printed structures was quantitatively evaluated using two key parameters: the Shape Fixing Rate (SFR) and the Shape Recovery Ratio (SRR). Further results and formulation are provided in Note S7 (Supporting Information).

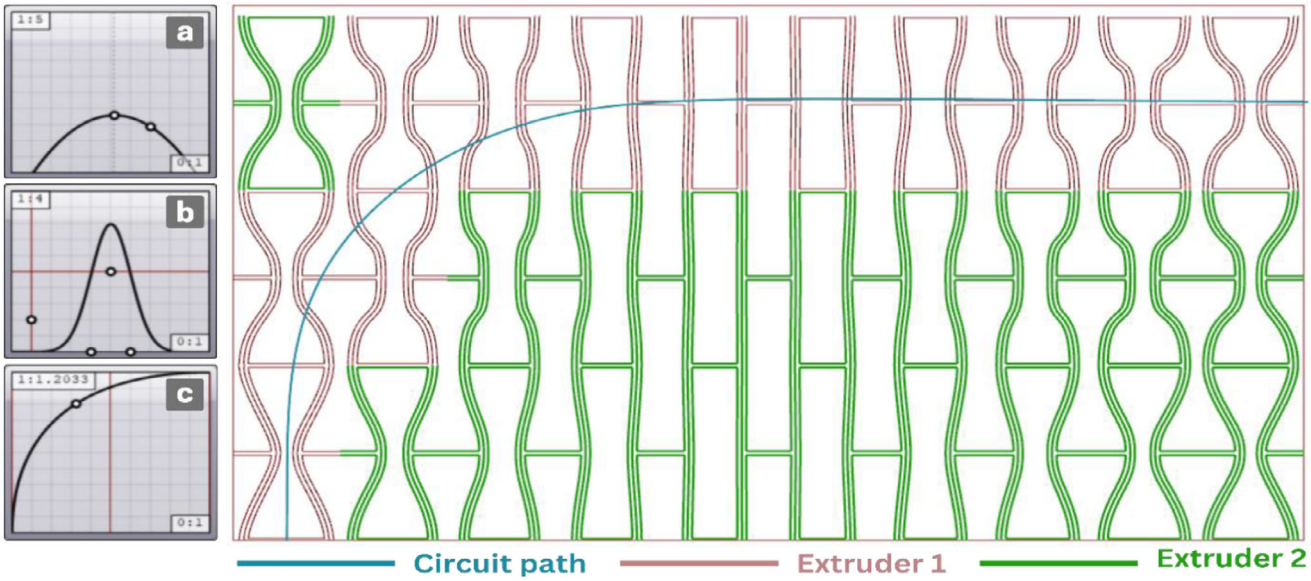

Figure 8. Adaptive dual-material circuit algorithm with user-defined circuit path and dynamic inputs: a) $\overline{V_1}$ along the x-direction, b) $\overline{V_2}$ along the x-direction, and c) $\overline{V_2}$ along the y-direction.

3. Adaptive Rotary Multi-Material Multi-Stimuli 4D Printing

To make a fully adaptive 4D auxetic structure, we propose an advancement to our algorithm by introducing variable inputs $\overline{V_1}$ and $\overline{V_2}$ as depicted in Figure 4. To make the whole algorithm more concise, we included the python scripting to ensure its reproducibility and further development which can be found in Algorithm S2 (Supporting Information).

To achieve a desirable and adaptive shape-morphing rotary auxetic structure, the algorithm is further advanced to independently generate a secondary path, allowing the creation of dual-responsive 4D material systems. As shown in **Figure 8**, this enhancement includes three dynamic inputs, each associated with a range of programmable curve functions. These include Bézier, bipolar, conic, Gaussian, linear, parabolic, Perlin, power, sigmoid-logit, sinc, sine, sine-summation, and square-root functions—offering a diverse and rich design space for dynamic adaptability.

As an experimental case study, we employed a straight-line path combined with three sine wave equations to demonstrate adaptive programming using two materials: thermoplastic elastomer (TPE) and iron-oxide PLA composites. This setup enabled multi-stimuli programming by leveraging the 4D printability of the selected materials. Detailed printing parameters, 4D adaptive auxetic cylindrical structure parameters, and selected input functions can be found in Note S8 (Supporting Information).

Additionally, the G-code files used for fabricating the adaptive auxetic 4D cylindrical structures are provided in G-code S1 (Supporting Information). A video demonstration of the printing process is available in Video S7 (Supporting Information).

Using the detailed printing parameters, we fabricated adaptive 4D multi-material, multi-stimuli cylindrical auxetic structures, as illustrated in **Figure 9**. To demonstrate the adaptive 4D

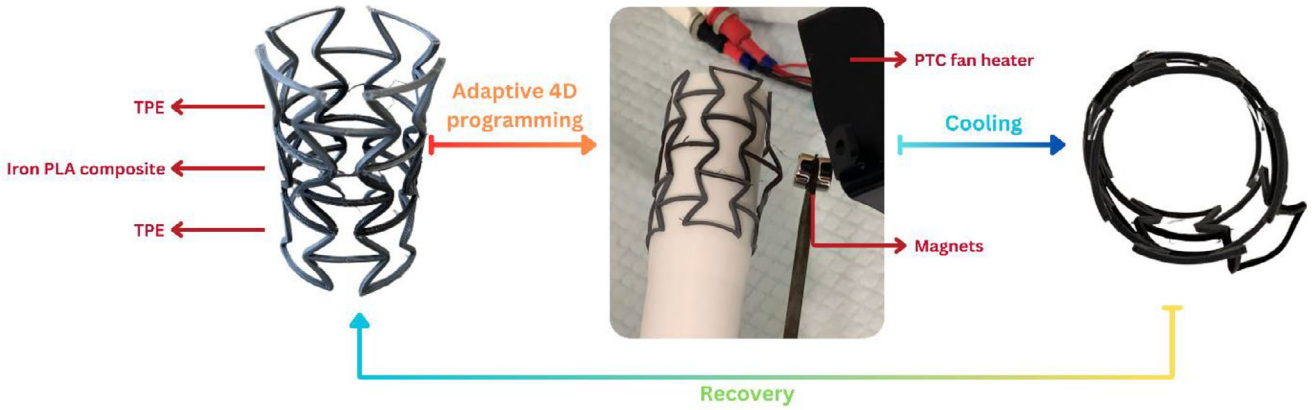

Figure 9. Adaptive 4D programming of multi-material multi-stimuli cylindrical re-entrant auxetic structure.

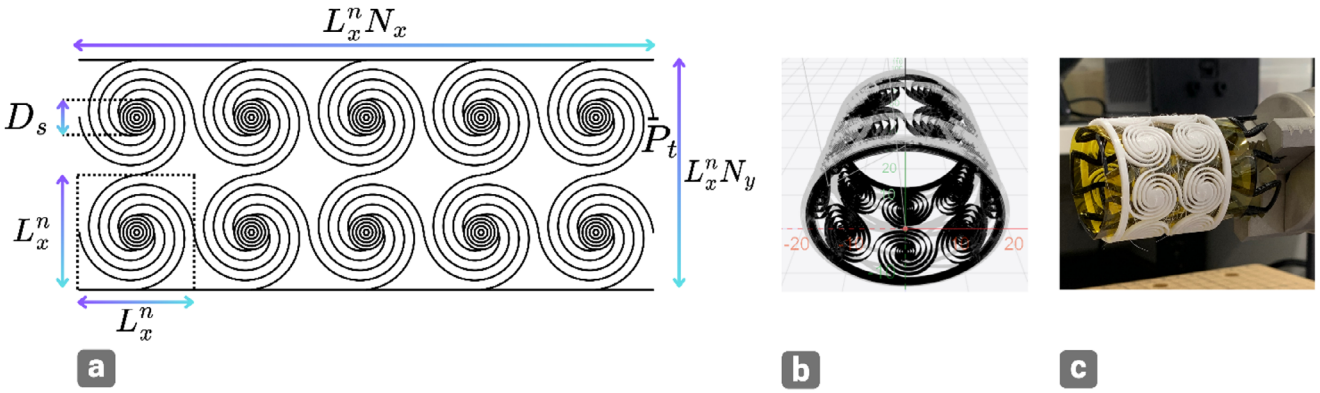

Figure 10. Novel Spiral Universal Joint. a) Workflow and input parameters for the spiral joint design algorithm. b) G-code simulation displayed in printer slicer software. c) Final PLA 3D-printed spiral universal joint on the 4D mandrel.

programming capabilities of our printing algorithm, we utilized stimulus-responsive materials—specifically leveraging a magnetic field to dynamically alter the auxetic cell patterns (Figure 9). Additionally, a PTC fan heater and a temperature gauge were used to heat the structures to the glass transition temperature of the iron-PLA composite, enabling shape deformation. A video demonstration of the programming process is available in Video S8 (Supporting Information). By combining this heating approach with a magnetic mask, the re-entrant auxetic structures could be selectively deformed into various programmable shapes. This non-planar 4D printing method is introduced here to the best of our knowledge, offering researchers a novel platform to explore diverse paths and strategies for programming complex auxetic geometries in 3D.

4. Rotary 4D Printing on a Rotary 4D Mandrel

To advance the development of a commercially viable, ready-to-use setup for hobbyist 3D printers, we propose an adaptable system capable of 3D printing tubular structures with variable diameters. This setup incorporates a flexible platform that allows for the adjustment of the platform diameter, enabling users to print on a wide range of cylindrical shapes and sizes. To achieve this, we introduce the use of auxetic metamaterials as a 4D mandrel. Auxetic materials exhibit a negative Poisson's ratio, enabling the rotary mandrel to expand or contract its diameter as needed during the printing process and subsequently return to its original shape after recovery with 4D programming. This reversible deformation enhances the versatility of the mandrel across different print geometries. To explore this feature, we examine the potential of the proposed setup to introduce innovative tubular structures, leveraging our algorithm and the rotary 4D mandrel, as discussed in the following section.

5. Parametric Tubular 4D Universal Spiral Joint

To fully investigate the potential applications of the proposed setup, we introduce a novel tubular 4D universal joint. Previously, such a design was impractical to fabricate without support structures and could not be printed in a continuous, uninterrupted path on a ready-to-use platform. This innovative approach leverages the unique capabilities of the setup to enable the seamless production of complex geometries, expanding the scope of 3D printing technologies in manufacturing functional, pre-assembled components.

A novel tubular 4D universal joint is proposed, as shown in **Figure 10**. The design algorithm, illustrated in Figure 10a, enables the creation of multiple spirals along the x and y directions. The flattened design is wrapped around the printing platform according to the 4D mandrel diameter, allowing for 3D printing across diverse diameters and achieving tunable stiffness along both the X and Y directions. Algorithm S3 (Supporting Information) provides further details on this algorithm, including the design of spiral shapes with customizable features and parameters, and additional insights about the spiral design algorithm are available in Note S9 (Supporting Information).

The generated G-code can be printed using the specified mentioned commercial 3D printer or any 3D printer capable of rotary motion, simulating printing paths as depicted in Figure 10b. The fully functional 4D mandrel is demonstrated by printing spiral joints on a rotary 4D mandrel, as shown in Figure 10c. Initially printed with a diameter of 30 mm, the 4D mandrel is then adjusted to a diameter of 35 mm. The parameters for the printed universal spiral joint are provided in Table S6 (Supporting Information). Additionally, the G-code files for the auxetic 4D mandrel and the universal spiral joint are provided in G-codes S2 and S3 (Supporting Information), respectively. A video demonstrating the printing process on the 4D mandrel is available in Video S9 (Supporting Information).

6. Results and Discussion

6.1. Bio-Inspired Parametric NURBS Re-Entrant Auxetic Metamaterials

In this study, we present a novel class of NURBS-based re-entrant auxetic metamaterials, inspired by the remarkable flexibility and control exhibited by bat wings (see Figure 1a). The proposed design algorithm facilitates the generation of a broad range of C^2-continuous curves, well-suited for diverse motions and 4D programming applications. These curves are parametrized by a combination of printing and geometric dimensions, and to accurately

characterize this class, we apply symbolic regression, achieving an exceptional R^2 accuracy of 0.9995. Using the resulting numerical equation, we derive a comprehensive model that accounts for all design parameters, enabling precise calculations of relative density and Poisson's ratio. These parameters are critical, as they directly influence the auxetic cells' shape-morphing behavior and their adaptive mechanical properties.

Through symbolic regression, we identified a novel parametric approach to derive a universal relation for calculating the relative density and Poisson's ratio for this class of curves. Given that a structure's mechanical properties are fundamentally tied to its relative density, and its deformation is strongly associated with its Poisson's ratio, this method enables an effective means of quantifying these attributes. Our findings confirm that the calculated relative density aligns within an acceptable range (0.05–0.95), validating the accuracy of the generated re-entrant auxetic NURBS. Furthermore, for optimal curve shapes and re-entrant configurations, it is recommended to aim for relative density values within a narrower range of 0.1–0.5.

Subsequently, we derived a parametric relation for Poisson's ratio, enabling the simulation of 4D cylindrical shells by capturing changes in diameter and deformation patterns. The results reveal an extensive range of Poisson's ratio values, from −0.5 to −15, highlighting significant auxetic potential. Notably, the maximum Poisson's ratio is achieved when the normalized offset value reaches 0.5, at which point the curves form fully straight lines. This simulation is provided in detail in Supplementary Algorithm S1.

6.2. Design-to-G-code Tubular Algorithm

Given that nonplanar printing of tubular structures has yet to reach commercialization, we propose a novel and fully parametric design-to-G-code algorithm, illustrated in Figures 3 and 8, which enables users to directly generate customized G-code for rotary 4D printing on any printer equipped with rotary motion capabilities. This algorithm was developed using Python scripting within the Grasshopper environment, ensuring reproducibility, extensibility, and full integration with user-defined auxetic designs. It also supports multi-material assignment along the toolpath, enabling fabrication of structures responsive to multiple external stimuli.

To support full adaptability, we further advanced the algorithm by introducing dynamic input variables $\overline{V_1}$ and $\overline{V_2}$, enabling the generation of dual-response paths for programmable material control. These paths can be defined by a library of curve functions including Bézier, conic, sigmoid-logit, sine, and Perlin curves, offering rich flexibility in designing morphing behavior. As a case study, we demonstrated the algorithm's practicality and reproducibility using an affordable, commercially available 3D printer, showcasing its ability to produce a wide variety of re-entrant tubular auxetic metamaterials efficiently and with no material waste. For instance, the provided G-code S1 (Supporting Information) was analyzed under two conditions: printed with planar slicing and using the rotary algorithm. The rotary approach resulted in a 70% reduction in material usage by eliminating the need for support structures. Additionally, printing time was reduced by nearly 50%, significantly lowering electricity consumption and labor requirements.

The algorithm was experimentally validated through the fabrication of adaptive structures using TPE and iron-oxide PLA composites. Using a combination of straight and sine-based dynamic paths, we demonstrated dual-material and dual-stimuli actuation capabilities—thermal and magnetic—within a single programmable tubular structure.

To further emphasize the sustainability aspect of this platform, and to align with circular energy goals, we explored the use of fully plant-based, biodegradable PLA filaments. In combination with iron-PLA composite filaments, this setup allows for dual-stimuli 4D programming—thermal and magnetic—within a single printed structure. This approach broadens the scope of 4D programming for tubular auxetic metamaterials, eliminating the need to print multiple geometries for different diameters and reinforcing environmentally conscious design practices.

6.3. Path Integration

To enhance the functionality of the tubular auxetic structure, we propose incorporating patterned paths, such as a zigzag trajectory, within our design-to-G-code algorithm as a demonstration. This addition broadens the structural adaptability and mechanical versatility of the auxetic design. By incorporating a zigzag path during the printing of auxetic cells, the concentration of stress is redistributed from the hinge areas to the broader structure. This redistribution mitigates the likelihood of localized failure, improving the overall structural durability, recovery rate, and extending the functional lifespan across multiple use cycles. As denoted in Figure 7, the incorporation of a zigzag path notably reduces the maximum Von Mises energy within the elements of the structure, indicating a significant decrease in localized stress concentrations. By examining 50 specimens, as detailed in previous sections, we observed an ≈15% reduction in maximum Von Mises stress when incorporating optimized fabrication paths for parametric re-entrant auxetic metamaterials. This stress reduction underscores the structural benefits of tailored path strategies in enhancing the mechanical resilience of these metamaterials.

To evaluate the mechanical influence of the zigzag path design, we applied a uniform linear pressure gradually increasing from 0 to 0.15 MPa on the inner surface of the structure to simulate 4D programming phase. In both the zigzag-path and path-free auxetic structures, we identified the maximum strain concentration point by analyzing the logarithmic strain (LE) field output across all nodes. The node exhibiting the highest principal strain at peak deformation was then selected for detailed strain energy analysis. As shown in **Figure 11**, the nodal strain energy at this critical point was consistently lower in the zigzag-path structure, exhibiting an average 36% reduction compared to the control configuration.

While the strain magnitude at these points was comparable between both designs, the strain energy was significantly lower in the zigzag-path case. This can be attributed to a more favorable stress distribution enabled by the compliant zigzag geometry, which reduces local stress concentrations and internal energy accumulation. Furthermore, the total strain energy of the entire structure, plotted over time in Figure 11, was found to be nearly

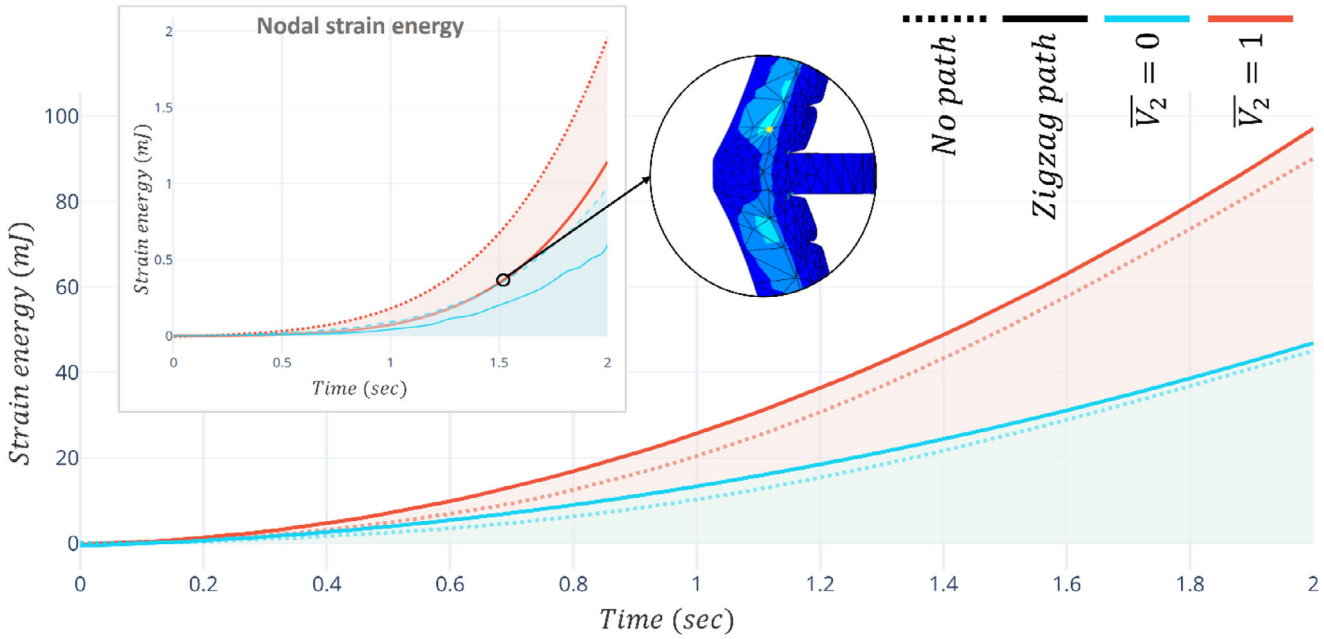

Figure 11. Nodal and total strain energy during 4D programming in zigzag-path and path-free auxetic structures. A uniform linear pressure (0–0.15 MPa) was applied to the inner surface. While total strain energy (≈100 mJ) is similar in both cases, the zigzag-path structure shows ≈36% lower nodal strain energy at the high-strain point, indicating improved local stress distribution.

identical between the two configurations ≈100 mJ at peak strain). This suggests that the zigzag-path structure maintains similar global energy absorption capacity, but redistributes strain energy more evenly across the network. This behavior underscores the mechanical efficiency of the zigzag design in mitigating localized deformation while preserving overall structural performance.

It is worth mentioning that to integrate auxetic patterns without leaving voids, a zigzag path was adopted. This configuration introduces multiple hinge-like regions that facilitate dissipation of stress concentrations. Importantly, we do not claim stress reduction; the zigzag path redistributes strain energy, shifting localized concentrations away from hinge regions while maintaining similar global absorption. As demonstrated in the nodal and global strain energy analysis (Figure 11), the zigzag-path design maintains a similar overall energy absorption capacity compared with the baseline, while shifting localized stress away from critical hinge regions. In practice, the fabricated path is not a sharp zigzag but a curved zigzag, as the finite nozzle radius (≈0.2 mm) naturally introduces fillets at the corners. This curvature mitigates sharp-edge effects and reduces the risk of stress concentration. Furthermore, zigzag trajectories are more straightforward to implement in G-code for rotary non-planar printing than fully curved paths, making them both a practical and mechanically robust solution for stress redistribution in 4D-printed auxetic structures.

6.4. Rotary 4D Mandrel

To facilitate the development of a commercially viable, ready-to-use system for hobbyist 3D printers, we propose an adaptable framework for 3D printing tubular structures with variable diameters. This system features a flexible platform with adjustable diameter settings, allowing users to print across a diverse range of cylindrical shapes and sizes. Central to this approach is the use of auxetic metamaterials as a rotary 4D mandrel. Auxetic materials as illustrated, possess a negative Poisson's ratio, which allows the mandrel to expand or contract as needed during printing, then recover its original dimensions upon release through 4D programming. This reversible deformation greatly enhances the mandrel's adaptability for a variety of print geometries.

Furthermore, the mandrel is fabricated using fully biodegradable materials, aligning with sustainability goals and promoting environmental responsibility. By employing such materials, the proposed setup facilitates the development of an entirely sustainable 3D printing platform. This solution not only meets the technical requirements of multi-diameter printing but also contributes to the reduction of material waste and supports significantly.

Finally, a user-friendly algorithm (Figure 3) is integrated into the system, allowing for the precise control and customization of printing parameters, such as diameter and shape. This algorithm enables seamless transitions between different cylindrical geometries, thereby simplifying the user experience and broadening the applicability of the system. In summary, this approach offers a sustainable and adaptable solution for 3D printing cylindrical structures, making it accessible to a wide range of users, researchers, and potential commercial markets.

6.5. Tubular 4D Universal Joint

To demonstrate the applicability of our developed tubular 3D/4D printing platform, we designed an innovative tubular structure

Table 2. 4D shape-morphing behavior of universal spiral joint specimens.

Sample	4D Axial Elongation		4D Rotational Deformation	
	SRR (%)	SFR (%)	SRR (%)	SFR (%)
I	98.6	90.2	95.2	87.2
II	98.3	89.6	91.2	81.6
III	96.7	87.2	85.0	86.7
IV	95.0	92.5	89.3	95.2
V	97.3	81.6	87.9	79.2
VI	98.9	84.9	94.5	81.0
VII	96.8	86.1	89.6	83.6
VII	97.1	93.0	97.8	90.9
IX	99.4	88.3	86.0	89.4
X	98.4	79.6	93.6	87.3
Average	97.6	87.3	91.0	86.2

that could not previously be manufactured without material waste or with commercially available ready-to-use printers. The proposed tubular 4D universal joint introduces a range of highly adaptable stiffnesses, encompassing axial, torsional, bending, and structural body stiffnesses, that allow for precise mechanical tuning, as denoted in Figure 10c and Video S10 (Supporting Information). This versatility enables tailored responses to environmental stimuli, making the joint an ideal candidate for applications where specific load-bearing or motion requirements are necessary.

The design also incorporates a shape recovery mechanism through 4D programming which enables the joint to revert to its original configuration after deformation, preserving its functional integrity across varied mechanical loads. This property underscores the material's robustness and durability, expanding its potential uses in scenarios that demand repeated shape adaptation without structural compromise. The shape programming process is briefly shown in Video S11 (Supporting Information). Additionally, after undergoing significant plastic deformation, the joints demonstrate an impressive capacity to nearly fully recover to their original shape, as illustrated in Video S12 (Supporting Information). Additionally, the programming and recovery behavior of the spiral structures was investigated using magnetic PLA composites, as demonstrated in Video S13 (Supporting Information).

To evaluate the 4D shape-morphing behavior of the universal spiral joints, a series of SRR and SFR tests were performed using 10 specimens. Each specimen was subjected to two separate 4D programming conditions: i) axial elongation of 1.5 mm along the longitudinal direction, and ii) rotational deformation with a 5° twist. The resulting SFR and SRR values for both conditions are summarized in **Table 2**. As indicated, the SFR values for both deformation scenarios were lower than 90%, in contrast to the higher SRR values. This can be attributed to the intrinsic geometric resilience of the universal spiral joints, which promotes partial recovery even during the fixation phase, causing the structure to resist the deformed shape and tend toward its original configuration.

To demonstrate the tunable stiffness capabilities of the universal spiral joints, a series of mechanical tests were conducted to evaluate their load-bearing capacity and overall mechanical performance. Two distinct spiral configurations were fabricated, as detailed in Table S7 (Supporting Information). These configurations differ in their pattern repetition along the X-direction, with one consisting of six spiral turns and the other eight. The comparative analysis aims to assess the influence of spiral repetition on stiffness and 4D deformation behavior under varied mechanical loading conditions. In this regard, two types of 4D programming were applied: one specimen was subjected to elongation of 1.5 mm along the Y-direction, while the other underwent a controlled rotation of 5 degrees. Further experimental details are provided in Note S10 (Supporting Information).

As illustrated in **Figure 12a**, specimens with a greater number of spirals exhibited higher axial stiffness. When the structures were 4D programmed through elongation along the longitudinal direction (1.5 mm), the axial stiffness remained largely unchanged. However, when programmed through rotational deformation (5° twist), a slight reduction in axial stiffness was observed.

Overall, the axial response of the spiral joints was predominantly linear and strongly influenced by both the number of spiral turns and the applied rotational deformation. These results demonstrate the potential for achieving dynamically tunable stiffness through structural design and multi-stimuli 4D programming. Additionally, the effect of contact between spiral ligaments was observed, particularly under 4D programming along the longitudinal direction. It was concluded that such deformation increases the displacement range significantly while maintaining nearly identical axial stiffness. This capability enables independent tuning of displacement range and mechanical response, offering a unique advantage for programmable spiral joints. By combining statistical design parameters—such as spiral count and pitch—with targeted 4D programming, the stiffness and deformation profile of the structure can be precisely controlled.

Similarly, experiments were conducted to evaluate the torsional stiffness of the universal spiral joints. As shown in Figure 12b, two distinct levels of linear torsional stiffness were achieved through variations in design parameters. Upon 4D programming of the spiral joints along the longitudinal direction, a significant reduction in torsional stiffness was observed. These results further confirm that a diverse and tunable stiffness range can be achieved through a combination of static design parameters and dynamic 4D programming. This dual approach enables programmable mechanical adaptability, making the spiral joint a promising candidate for applications requiring variable compliance or stiffness modulation.

Finally, a similar experiment was conducted to characterize the overall structural behavior of the cylindrical spiral assembly. As shown in Figure 12c, the load capacity and range of motion of individual spirals within the structure closely match the axial response of the entire system. The results indicate that the cubic nonlinear, contactless behavior of each spiral is consistent across the structure and can be effectively tuned through both geometric design parameters and 4D programming. This flexibility enables a broad range of structural damping and stiffness responses to be embedded within a single universal spiral joint, offering dynamic mechanical adaptability through minimal material and design changes.

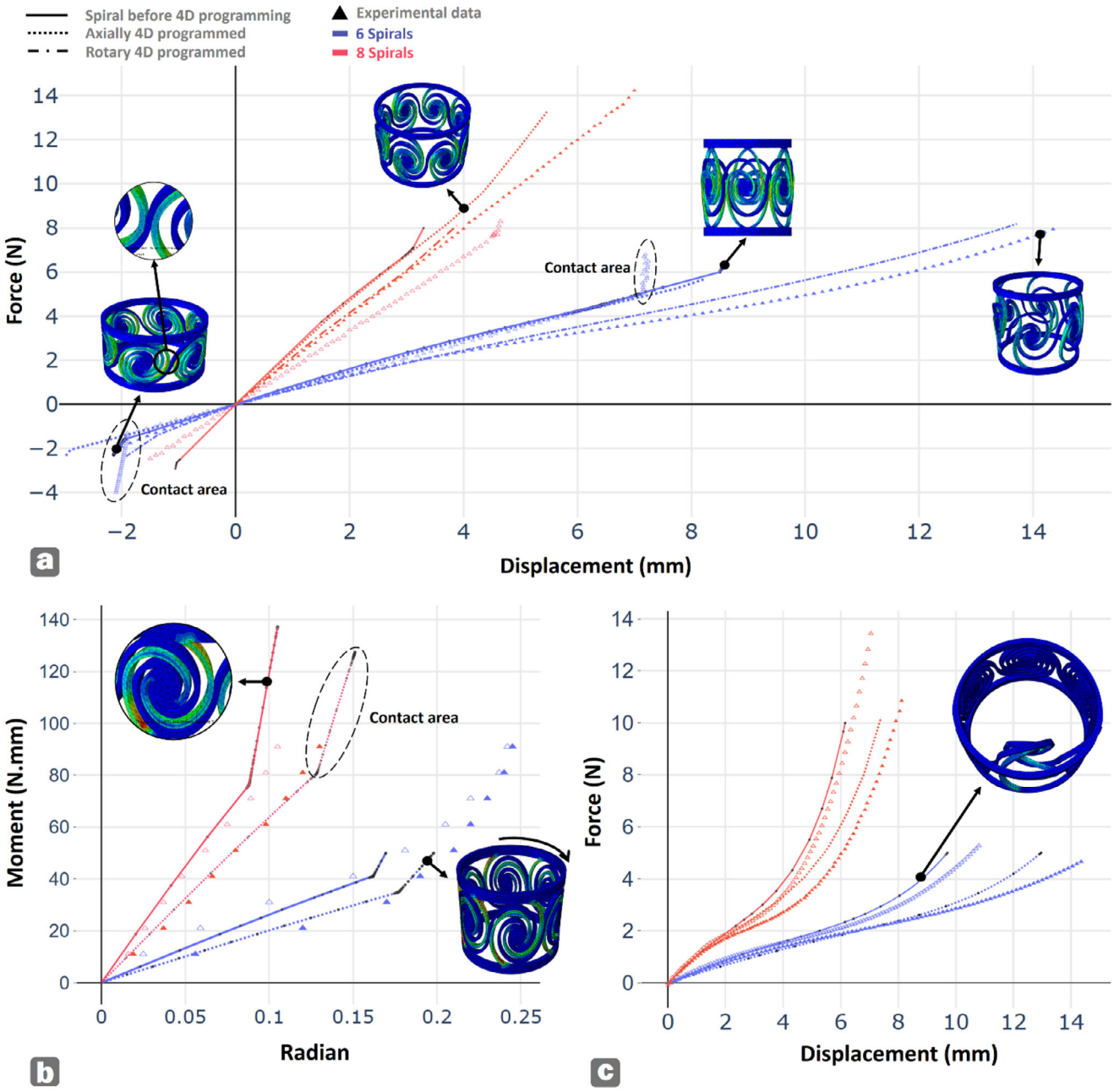

Figure 12. Experimental and finite element analysis of the axial, torsional, and structural stiffness of cylindrical spiral structures with 6 and 8 turns, evaluated before and after 4D programming. Data shown as mean ± SD from n = 2 independent specimens (six repeats each; specimen-level means used). No formal hypothesis testing was performed. a) Axial stiffness where results include both Instron tensile testing and FEM simulation to quantify stiffness modulation due to shape-morphing behavior. b) Torsional stiffness results obtained from both rotary motion sensor experiments and FEM simulations, used to quantify stiffness modulation induced by shape-morphing behavior. c) Structural stiffness results obtained from Instron tensile testing and FEM simulations, highlighting changes in stiffness due to the programmed deformation.

These 4D tubular universal joints hold strong potential for soft robotics, where 4D programming enables the tuning of joint characteristics to achieve diverse functional behaviors. While a comprehensive characterization of these 4D universal joints is beyond the scope of this paper and warrants a separate study, we demonstrate several potential applications that merit further exploration. Video S14 (Supporting Information) highlights how these structures serve as robotic joints with multi-DOF capabilities and effective energy-damping properties. Additionally, a small-scale experiment in Video S15 (Supporting Information) illustrates how programming the structure (as shown in Video S11, Supporting Information) impacts the overall bending stiffness of the robotic joint. Video S16 (Supporting Information) provides a case study demonstrating how larger, tunable spiral

structures can enhance stability and dissipate unwanted energy. These spirals, designed through 4D programming, exhibit versatile features that allow for adaptability across various environments. Their tunable nature enables them to adjust dynamically, making them suitable for applications requiring responsive stabilization and energy damping.

Moreover, the use of biodegradable materials in these joints aligns with sustainable engineering principles and supports a circular economy. By focusing on material degradation post-use, the joint's design contributes to environmental conservation, minimizing waste and ecological footprint in line with the United Nations' sustainability goals. Such material properties not only provide scientific advantages but also ensure that the applications of these 4D-printed structures support both technological advancement and environmental responsibility.

This study presents a comprehensive framework for adaptive, sustainable, and programmable rotary 4D printing. The key innovations and contributions are summarized below:

- **A novel rotary 4D fabrication platform**, integrating adaptive geometric design with non-planar toolpaths, enabling direct and automated G-code generation from diverse 2D and 3D geometrical inputs for tubular structures.
- **An open-source, Python-based rotary slicing algorithm**, implemented in the Grasshopper environment, capable of generating non-planar, multi-material, multi-stimuli G-code paths. The algorithm is freely accessible and reproducible rotary 4D slicer available for the broader research and maker community.
- **A continuous-path, fiber-like deposition strategy**, replacing conventional layer-by-layer printing to improve mechanical performance, reduce material waste, and eliminate the need for support structures in tubular geometries.
- **A dual-material, multi-stimuli design approach**, demonstrated through the use of biodegradable PLA and iron-PLA composites, enabling dynamic 4D actuation via both thermal and magnetic stimuli.
- **A dual-path programming logic**, allowing users to define shape-morphing behavior using programmable mathematical functions (e.g., sine, sigmoid, Bézier), enabling deformation control through dynamic inputs.
- **Advanced material modeling**, incorporating hyperelastic and thermoelastic responses via user-defined subroutines in Abaqus and validated through high-strain FEM simulations.
- **Integration of zigzag paths for stress redistribution**, introduced as a geometry-aware design feature not available in commercial or open-source slicers. FEM and experimental validation showed a 36% reduction in local strain energy, significantly improving structural resilience.
- **A data-driven predictive module**, linking input geometries and material configurations to final 4D deformation outcomes. This approach reduces reliance on repeated FEM simulations and introduces a theoretical contribution to programmable structure design. Symbolic regression-based modeling of re-entrant NURBS auxetic geometries with high accuracy (R^2 = 0.9995), providing a predictive link between design and shape-morphing behavior.
- **Experimental realization of a tunable universal spiral joint**, capable of programmable stiffness modulation under axial, torsional, and structural loads, highlighting the adaptability of the proposed platform for use in robotics, biomedical devices, and reconfigurable mechanical systems.
- **Conceptualization and demonstration of a 4D self-morphing mandrel**, which serves not only as a programmable base structure but also as a fabrication scaffold for non-planar printing of complex geometries—extending the functional scope of 4D printing into new application domains.

7. Statistical Analysis

Experimental data are reported as mean ± SD. For Figure 6b, n = 3 independent specimens; the dot–dash line connects specimen-level measurements of experimental results. For Figure 12, n = 2 independent specimens, each tested in six repeated trials; the unit of analysis is the specimen (trial measurements averaged per specimen). No data were excluded and no outliers were removed. Because this work primarily demonstrates a fabrication/design pipeline and sample sizes are small, no formal hypothesis testing was performed; differences are descriptive. Analyses were performed in Python (NumPy/SciPy) and figures prepared in Matplotlib.

8. Conclusion

In conclusion, we have developed an innovative and open-source design-to-G-code algorithm that enables the generation of customizable toolpaths for diverse tubular structures using commercially available, affordable 3D printers. This platform facilitated the fabrication of bio-inspired, parametric NURBS-based re-entrant auxetic metamaterials, forming the basis for a novel rotary 4D mandrel design. Symbolic regression was employed to model these complex curves with high precision (R^2 = 0.9995), enabling accurate geometry-driven deformation behavior. To promote sustainable and material-efficient tubular 4D printing, the rotary mandrel was enhanced with an auxetic skin and embedded zigzag pathing to mitigate stress concentrations and improve mechanical resilience across varying diameters. The entire slicing and programming pipeline was implemented using Python scripting within the Grasshopper environment and extended to support multi-material, multi-stimuli actuation. These capabilities were demonstrated through both thermal and magnetic stimuli using biodegradable PLA and iron-PLA composites. Comprehensive FEM and experimental studies validated the tunable stiffness of the printed structures, revealing how 4D programming and design parameters together enable fine-grained mechanical control. Finally, to showcase the platform's full potential, we developed adaptive tubular 4D universal spiral joints with programmable, multi-directional stiffness. These joints exhibited dynamic response under axial, torsional, and structural loading, proving the system's versatility for applications ranging from robotics and aerospace to biomedical engineering. To the best of our knowledge, this work introduces a novel 4D printing system that adaptively reconfigures based on its fabrication logic—establishing a modular, programmable platform for non-planar 4D printing across a wide range of sectors.

Supporting Information

Supporting Information is available from the Wiley Online Library or from the author.

Acknowledgements

A.Z. acknowledges the support by the Australian Research Council (ARC) under the Discovery Early Career Research Award (DECRA) [Project No. DE240100960] funded by the Australian Government. Mahdi Bodaghi acknowledges the support by the UK Engineering and Physical Sciences Research Council (EPSRC) (Award No. EP/Y011457/1, I5M project). This research is supported by Australian Research Council [Project No. DE240100960] funded by the Australian Government.

Conflict of Interest

The authors declare no conflict of interest.

Authors Inclusion and Ethics Statement

All authors have contributed equally to the study and approved the final manuscript. The research was conducted in accordance with ethical standards and responsible research practices.

Data Availability Statement

The data that support the findings of this study are available in the supplementary material of this article.

Keywords

4D mandrel, 4D printing, cylindrical auxetic metamaterials, multi-stiffness universal joints, rotary 3D printing

Received: July 27, 2025
Revised: September 5, 2025
Published online:

[1] M. Mehrpouya, H. Vahabi, S. Janbaz, A. Darafsheh, T. R. Mazur, S. Ramakrishna, *Polymer* **2021**, *230*, 124080.
[2] F. Momeni, X. Liu, J. Ni, *Mater. Des.* **2017**, *122*, 42.
[3] M. Bodaghi, L. Wang, F. Zhang, Y. Liu, J. Leng, R. Xing, M. D. Dickey, S. Vanaei, M. Elahinia, S. V. Hoa, D. Zhang, K. Winands, T. Gries, S. Zaman, H. Soleimanzadeh, T. B. Palmić, J. Slavič, Y. Tadesse, Q. Ji, C. Zhao, L. Feng, K. Ahmed, M. N. I. Shiblee, *Smart Mater. Struct.* **2024**, *33*, 113501.
[4] A. Valipour, M. H. Kargozarfard, M. Rakhshi, A. Yaghootian, H. M. Sedighi, *J. Mater.: Design Appl.* **2022**, *236*, 2171.
[5] R. Hamzehei, M. Bodaghi, N. Wu, *Smart Mater. Struct.* **2024**, *33*, 083001.
[6] Z. Li, W. Gao, N. Kessissoglou, S. Oberst, M. Y. Wang, Z. Luo, *Mater. Des.* **2023**, *232*, 112146.
[7] T. Tabassum, A. A. Mir, *Mater. Today: Proc.* **2023**, *93*, 408.
[8] X. Zheng, X. Guo, I. Watanabe, *Mater. Des.* **2021**, *198*, 109313.
[9] M. Bodaghi, A. R. Damanpack, W. H. Liao, *Smart Mater. Struct.* **2016**, *25*, 105034.
[10] R. Hamzehei, M. Bodaghi, J. A. Iglesias Martinez, Q. Ji, G. Ulliac, M. Kadic, C. Wang, A. Zolfagharian, N. Wu, *Adv. Eng. Mater.* **2023**, *25*, 2201842.
[11] R. Hamzehei, A. Serjouei, N. Wu, A. Zolfagharian, M. Bodaghi, *Adv. Eng. Mater.* **2022**, *24*, 2200656.
[12] M. Wan, K. Yu, H. Sun, *Compos. Struct.* **2022**, *279*, 114791.
[13] A. Le Duigou, M. Grabow, F. Scarpa, J. Deschamps, C. Combescure, K. Labstie, J. Dirrenberger, M. Castro, U. Lafont, *Adv. Mater. Technol.* **2025**, *10*, 2400237.
[14] M. Josselin, M. Castro, N. Di Cesare, F. Scarpa, A. L. Duigou, *Adv. Mater.* **2025**, *37*, 2418656.
[15] O. Byrne, F. Coulter, M. Glynn, J. F. X. Jones, A. Ní Annaidh, E. D. O'Cearbhaill, D. P. Holland, *Soft Rob.* **2018**, *5*, 726.
[16] A. J. Guerra, J. Ciurana, *Mater. Des.* **2018**, *137*, 430.
[17] D. Zhao, R. Zhou, J. Sun, H. Li, Y. Jin, *Polym. Eng. Sci.* **2019**, *59*, 1122.
[18] G. Singh, R. Paetzold, F. Coulter, C. J. McMahon, K. Walsh, W. Ronan, E. O'Cearbhaill, *Proc. CIRP* **2022**, *110*, 156.
[19] Z.-P. Wang, L. H. Poh, *Compos. Struct.* **2018**, *201*, 486.
[20] Z.-P. Wang, L. H. Poh, Y. Zhu, J. Dirrenberger, S. Forest, *Mater. Des.* **2019**, *170*, 107669.
[21] J. Li, D. K. Pokkalla, Z.-P. Wang, Y. Wang, *Eng. Struct.* **2023**, *292*, 116477.
[22] G. Hu, M. Bodaghi, *Adv. Eng. Mater.* **2023**, *25*, 2300334.
[23] T. Van Manen, S. Janbaz, A. A. Zadpoor, *Mater. Horiz.* **2017**, *4*, 1064.
[24] F. Zhang, N. Wen, L. Wang, Y. Bai, J. Leng, *Int. J. Smart Nano Mater.* **2021**, *12*, 375.
[25] S. Pothier, R. Roufail, M. Malton, *J. Minerals Mater. Characteriz. Eng.* **2022**, *10*, 360.
[26] R. Gomes, L. A. d. Oliveira, M. B. Francisco, G. F. Gomes, *Smart Mater. Struct.* **2024**, *33*, 085010.
[27] H. Soleimanzadeh, B. Rolfe, M. Bodaghi, M. Jamalabadi, X. Zhang, A. Zolfagharian, *Adv. Sustainable Syst.* **2023**, *7*, 2300289.
[28] A. Alomarah, Z. A. Al-Ibraheemi, D. Ruan, *Smart Mater. Struct.* **2023**, *32*, 115028.
[29] M. Abbaslou, R. Hashemi, E. Etemadi, *Mater. Today Commun.* **2023**, *35*, 105742.
[30] A. Zolfagharian, M. Bodaghi, R. Hamzehei, L. Parr, M. Fard, B. F. Rolfe, *Sustainability* **2022**, *14*, 6831.
[31] H.-G. Choi, S. Pyo, J.-W. Choi, K. Park, *Adv. Eng. Mater.* **2025**, *27*, 2400889.
[32] L. Piegl, *Comput.-Aided Design* **1989**, *21*, 509.
[33] X. Zhang, J. Wang, Q. Sun, J. Li, S. Zhou, J. Qi, R. Tao, *Int. J. Smart Nano Mater.* **2024**, *15*, 1.
[34] M. F. Simons, K. M. Digumarti, A. T. Conn, J. Rossiter, *Tiled Auxetic Cylinders for Soft Robots*, IEEE, Piscataway, New Jersey, **2019**.
[35] F. Liu, Y. Song, H. Liu, B. Zhang, *Int. J. Crashworthiness* **2024**, *29*, 726.
[36] T. Wang, J. An, H. He, X. Wen, X. Xi, *Compos. Struct.* **2021**, *262*, 113663.
[37] H. Hai, C. Chen, W. Wang, W. Xu, *Phys. Scr.* **2024**, *99*, 025919.
[38] R. Afshar, S. Jeanne, B. E. Abali, *Appl. Compos. Mater.* **2023**, *30*, 987.
[39] V. T. Endo, J. C. C. Pereira, *Mech. Time-Dependent Mater.* **2017**, *21*, 199.
[40] O. H. Yeoh, *Rubber Chem. Technol.* **1993**, *66*, 754.
[41] J. Shojaeiarani, M. Hosseini-Farid, D. Bajwa, *Mech. Mater.* **2019**, *135*, 77.
[42] T. Van Manen, S. Janbaz, A. A. Zadpoor, *Mater. Today* **2018**, *21*, 144.